Texture Variation Adaptive Image Denoising With Nonlocal PCA

Wenzhao Zhao, Qiegen Liu, *Member, IEEE*, Yisong Lv, and Binjie Qin, *Member, IEEE*

***Abstract*— Image textures, as a kind of local variations, provide important information for the human visual system. Many image textures, especially the small-scale or stochastic textures, are rich in high-frequency variations, and are difficult to be preserved. Current state-of-the-art denoising algorithms typically adopt a nonlocal approach consisting of image patch grouping and group-wise denoising filtering. To achieve a better image denoising while preserving the variations in texture, we first adaptively group high correlated image patches with the same kinds of texture elements (texels) via an adaptive clustering method. This adaptive clustering method is applied in an over-clustering-and-iterative-merging approach, where its noise robustness is improved with a custom merging threshold relating to the noise level and cluster size. For texture-preserving denoising of each cluster, considering that the variations in texture are captured and wrapped in not only the between-dimension energy variations but also the within-dimension variations of PCA transform coefficients, we further propose a PCA-transform-domain variation adaptive filtering method to preserve the local variations in textures. Experiments on natural images show the superiority of the proposed transform-domain variation adaptive filtering to traditional PCA-based hard or soft threshold filtering. As a whole, the proposed denoising method achieves a favorable texture-preserving performance both quantitatively and visually, especially for irregular textures, which is further verified in camera raw image denoising.**

***Index Terms*— Texture-preserving denoising, adaptive clustering, principal component analysis transform, suboptimal Wiener filter, LPA-ICI.**

I. Introduction

TEXTURE, as a systematic local variation of image values, is an essential component of natural visual information reflecting the physical properties of the surrounding environment [1]. There are two basic types of texture pattern:

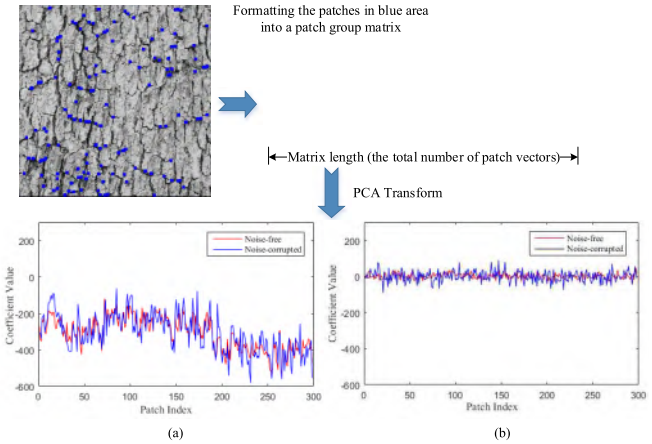

Fig. 1. The between- and within-dimension variations of PCA trans-

- Besides of additive Gaussian noise reduction, the proposed denoising method is applied to remove Poisson-Gaussian noise in the camera raw image.

The rest of the paper is organized as follows. In Section II we introduce the noise model. Section III, IV and V are about the details of the adaptive patch clustering, texture variation adaptive filtering for PCA coefficients and the sliding window and aggregation technique, respectively. Experimental results are displayed in Section VI. Finally, conclusion is given in Section VII.

II. Noise Model

The additive white Gaussian noise (AWGN) is written as:

$$y = x + n, \tag{1}$$

where x is noise-free data, y is noisy, and n follows the normal distribution with zero mean and variance σ^2. AWGN is signal-independent.

Being different from AWGN, the Poisson-Gaussian noise corrupting the camera raw images that are acquired from digital cameras is typically signal-dependent noise. Let x be a noise-free signal at the position c. The observed data with Poisson-Gaussian noise can be written as:

$$y(\mathbf{c}) = \rho/\alpha + b\upsilon, \tag{2}$$

where $\rho \sim P(\alpha(x(\mathbf{c}) - p))$ is a Poisson variable with the parameter $\alpha(x(\mathbf{c}) - p)$, υ follows the normal distribution $N(0, 1)$, and α, b, p are parameters of the Poisson-Gaussian noise.

After applying a variance stabilization transform for the signal-dependent Poisson-Gaussian noisy signal, we can remove the noise using the denoising methods for additive white Gaussian noise. One well-known variance stabilization transform is called generalized Anscome transform (GAT) [26], [27]. GAT can approximately transform Poisson-Gaussian noise into additive white Gaussian noise with unitary variance:

$$f(y) = \begin{cases} 2\sqrt{y' + \frac{3}{8} + \sigma'^2}, & y' > -\frac{3}{8} - \sigma'^2 \\ 0, & y' \le -\frac{3}{8} - \sigma'^2 \end{cases} \tag{3}$$

where $y' = \alpha y$ and $\sigma' = \alpha b$.

Let x be the noise-free data, and the denoised data is treated as $E[f(y)|x]$. The exact unbiased inverse of the GAT is defined as:

$$T($$

clusters according to a custom threshold. To this end, there are two problems that need to be solved:

a) clustering a huge number of clusters requires a huge computational burden due to the high dimensionality of image patches;
b) finding a way to calculate a suitable merging threshold for merging similar clusters.

For the first problem, we adopt the divide and conquer technique [28], [29]. The divide and conquer technique is a two-stage clustering scheme, which accelerates the K-means clustering with improved performance: It first clusters a small number of clusters using K-means, and then within each cluster it performs the K-means clustering again to further increase the cluster number.

For the second problem, we derive the merging threshold on the distance of any two similar clusters according to the noise level and cluster size. Specifically, we consider one special case, where we have two similar clusters $\mathbf{A} \in \mathbb{R}^{M \times L_a}$ and $\mathbf{B} \in \mathbb{R}^{M \times L_b}$ with very different sizes $L_a \gg 1$ and $L_b = 1$. Supposing the noise variance in the center of the large cluster $\mathbf{A}$ is small enough to be ignored, we further denote by $\mathbf{y}_a = \mathbf{x}$ and $\mathbf{y}_b = \mathbf{x} + \mathbf{n}$ the centers of $\mathbf{A}$ and $\mathbf{B}$ respectively, where $\mathbf{x}$ is noise-free, and the entries n

Algorithm 1 Adaptive Clustering Via Over-Clustering and Iterative Merging

Input:

detection has been used in some image denoising algorithms such as SADCT [20] and BM3DSAPCA [8], to adaptively detect the spatial variations of image value and collect similar pixel samples. However, the proposed algorithm uses LPA-ICI for signal variation detection in the PCA transform-domain.

Standard linear LPA tries to fit the signal $y(n)$ locally with polynomial functions of order m. Here, since we only use it to detect variations and find neighborhood with high internal similarity, we simply apply the zero-order polynomial fitting ($m = 0$) to find a suitable window of size h (a window containing $N_h = 2h + 1$ data points) where all the similar signal in the window can be approximated by a constant amplitude signal $\hat{y}(n, h) = C$. The computation of $\hat{y}(n, h)$ in LPA is related to the following loss function:

$$\Im_h(n) = \frac{1}{N_h} \sum_{s=1}^{N_h} \rho_h(n_s - n)(y(n_s) - \hat{y}(n, h))^2 \qquad (10)$$

where $y(n_s)$, $1 \le s \le N_h$ is the signal at the point in a window of size h with n as its center, $\rho(\cdot)$ is a basic window function, and $\rho_h(\cdot) = \rho(\cdot/h)/h$. For simplicity, we use the square uniform window, where $\rho(\cdot) = 1$ in $[-1, 1]$, and $\rho(\cdot) = 0$, otherwise. So there is $\rho_h(\cdot) = 1/h$ in $[-h, h]$, and $\rho(\cdot) = 0$, otherwise.

For a certain window size h, by minimizing the loss function, we have the estimate of $y(n)$: $\hat{y}(n, h) = \frac{1}{N_h} \sum_{s=1}^{N_h} y(n_s)$ and its standard deviation $std(n, h) = \frac{\sigma}{\sqrt{N_h}}$. So the confidence interval of the estimate can be

$$\begin{aligned} D &= [L, U] \\ U &= \hat{y}(n, h) + \Gamma \cdot std(n, h) \\ L &= \hat{y}(n, h) - \Gamma \cdot std(n, h) \end{aligned} \qquad (11)$$

where Γ is a threshold parameter.

Given a finite set of window size $H = h_1 < h_2 < \cdots < h_J$ starting from the minimum window size h_1, for each window we can use the LPA to get a estimate $\hat{y}(n, h_i)$ and a corresponding standard deviation $std(n, h_i)$, thereby determining a sequence of the confidence intervals $D(i)$, $1 \le i \le J$ of the biased estimates:

$$\begin{aligned} D(i) &= [L_i, U_i] \\ U_i &= \hat{y}(n, h_i) + \Gamma \cdot std(n, h_i) \\ L_i &= \hat{y}(n, h_i) - \Gamma \cdot std(n, h_i) \end{aligned} \qquad (12)$$

The ICI technique considers the optimal h to be the maximum window length satisfying $\underline{L_i} < \overline{U_i}$, where

$\upsilon_{sd}(g_s) \triangleq \frac{E\{[f(n)-h_s f(n)]^2\}}{\sigma_f^2}$, and the noise-reduction index is $\xi_{nr}(h_s) \triangleq \frac{\sigma_w^2}{E\{[h_s w(n)]^2\}}$.

Then, we can obtain the optimal α by maximizing the following discriminative cost function related to the noise-reduction and signal-distortion indexes [24],

$$J(\alpha) \triangleq \frac{\xi_{nr}(h_s)}{\xi_{nr}(h_o)} - \beta \frac{\upsilon_{sd}(g_s)}{\upsilon_{sd}(g_o)} = \frac{\sigma^2 + g_o R_w g_o - 2\sigma^2 g_o}{\sigma^2 + \alpha^2 g_o R_w g_o - 2\alpha\sigma^2 g_o} - \beta\alpha^2, \quad (17)$$

where β is an application-dependent constant and determines the relative importance between signal preservation and noise reduction. When β becomes larger, we have less signal distortion with less noise removal. We set $\beta = 0.7$ as in [24] to achieve a good balance.

With the suboptimal Wiener filter above, we tackle each $\mathbf{p}_i$ from $\mathbf{P}_R$

THE AVERA WITH NT

σ			00,0.5)	00,0.7)
			2.50	
	FSIM	0.9141	0.9152	

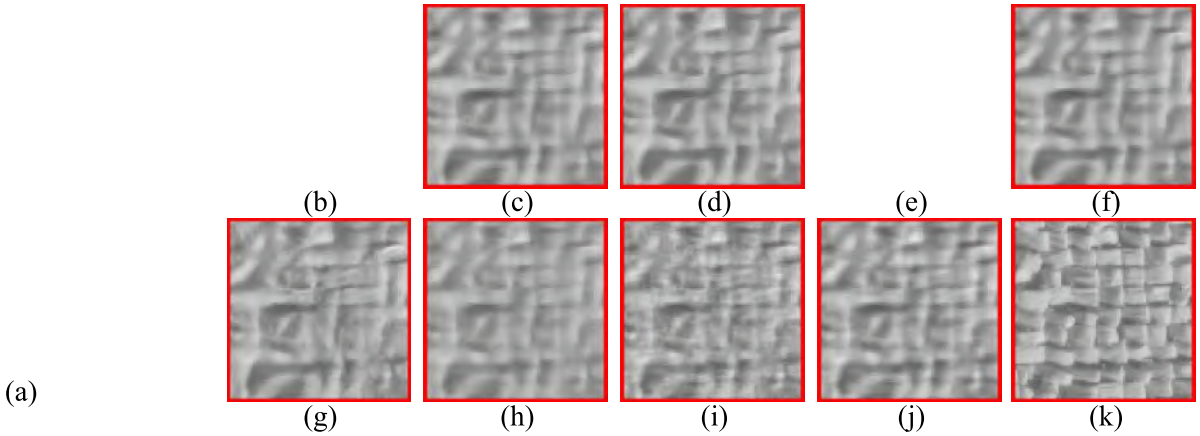

Fig. 9. Denoising the Grid image at $\sigma = 50$: (a) Grid image, (b) Noisy block, (c) BM3D, (d) BM3DSAPCA, (e) WNNM, (f) SLRD, (g) DnCNN-S, (h) SGHP, (i) AC-PT, (j) ACVA, (k) Noise-free block.

TABLE III

THE AVERAGE PSNR(dB), SSIM, FSIM RESULTS ON 16 IMAGES WITH IRREGULAR TEXTURES FROM THE USC-SIPI DATASET

Methods	σ	10	20	30	40	50

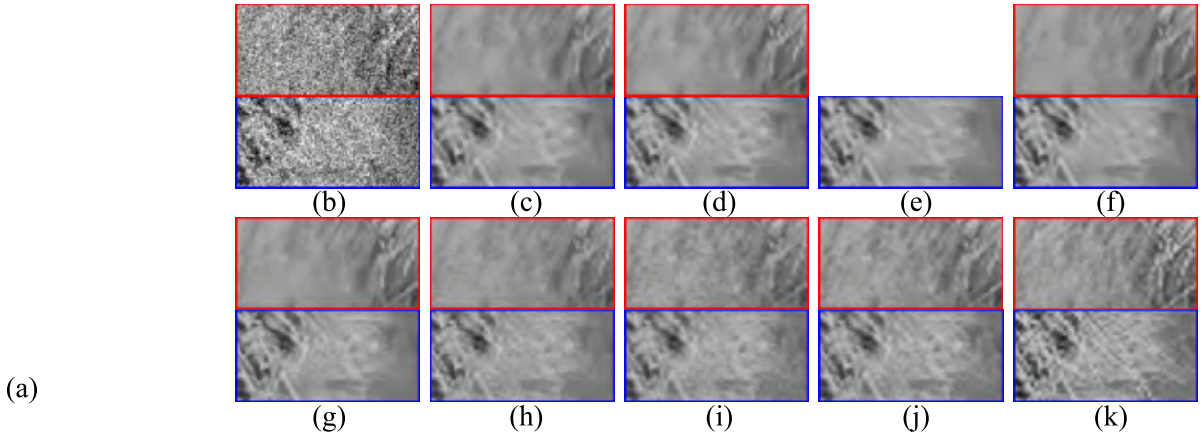

Fig. 10. Denoising the Mandrill image at $\sigma = 30$ with image details in the zoomed areas (red and blue boxes): (a) Mandrill image, (b) Noisy block, (c) BM3D, (d) BM3DSAPCA, (e) WNNM, (f) SLRD, (g) DnCNN-S, (h) SGHP, (i) AC-PT, (j) ACVA, (k) Noise-free block.

it can be observed that the proposed method outperforms other methods in restoring the textures of the fur (in Fig. 10) and water surface (in Fig. 11).

B. Camera RAW Image Denoising

1) Camera RAW Image Simulation: Four standard RGB test images, specifically, Peppers, Lena, Baboon, and House are selected for camera raw image denoising simulation. We adopt the simulation method used in [46]. To transform the RGB images into simulated raw images, we first scale the RGB images (within the bounds of $[0, 1]$) to the domain of raw images:

$$[r'_{i,j}, g'_{i,j}, b'_{i,j}]^T = R_{max} \times [r_{i,j}, g_{i,j}, b_{i,j}]^T \tag{19}$$

where r, g, and b denote the signal in red, green, and blue channels, respectively, i and j are the x-coordinate and y-coordinate of any image pixel, respectively.

Then the pixels are further arranged into four subimages, R, $G1$, $G2$, and B for simulation of the color filter array (CFA) [47].

$$\begin{aligned} R &= \{r''_{i,j} = r'_{2i-1,2j-1}\}, \\ G1 &= \{g''_{i,j} = g'_{2i-1,2j}\}, \\ G2 &= \{g''_{i,j} = g'_{2i,2j-1}\}, \\ B &= \{b''_{i,j} = b'_{2i,2j}\}. \end{aligned} \tag{20}$$

Finally, all the four subimages are arranged into a single image to simulate the RAW image.

To better simulate the noise in the real RAW image, we set the noise parameters $\alpha > 0$, $b = 0$, $p = 0$ as [46]. Based on Poisson-Gaussian noise reduction scheme described in Section II, we apply the proposed algorithm to denoise R, G1, G2, and B separately and then compute the average PSNR (SSIM and FSIM) results for evaluation.

Table V compares the quantitative performance of nine competing algorithms on simulated camera RAW images. We can see that the proposed algorithm is superior to all other algorithms in terms of SSIM and FSIM on average.

TABLE V

PSNR (dB), SSIM, FSIM RESULTS OF CAMERA RAW IMAGE SIMULATION ON THE RGB IMAGES SHOWN IN FIG. 7

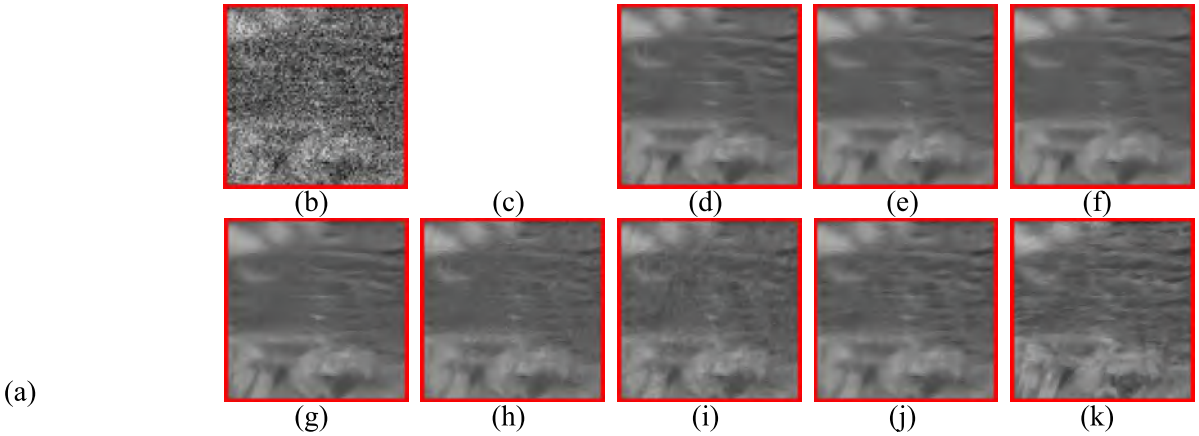

Fig. 11. Denoising the Stream image at $\sigma = 25$ with image details in the zoomed areas (red boxes): (a) Stream image, (b) Noisy block, (c) BM3D, (d) BM3DSAPCA, (e) WNNM, (f) SLRD, (g) DnCNN-S, (h) SGHP, (i) AC-PT, (j) ACVA, (k) Noise-free block.

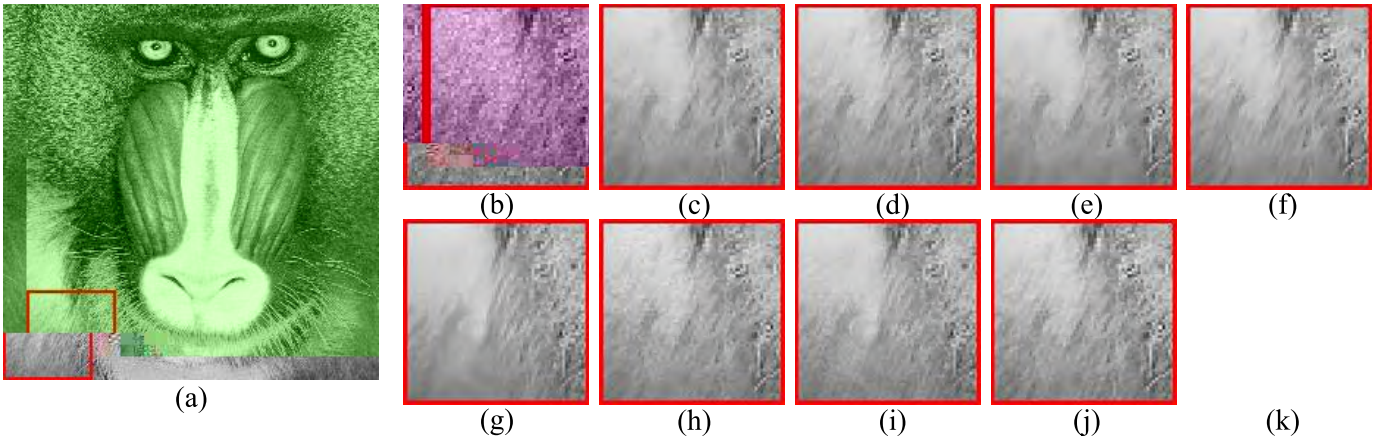

Fig. 12. Performance comparison on the red channel of Baboon image with image details in the zoomed areas (red boxes): (a) The red channel, (b) Noisy block ($\alpha = 200$), (c) BM3D, (d) BM3DSAPCA, (e) NCSR, (f) WNNM, (g) DnCNN-S, (h) SGHP, (i) AC-PT, (j) ACVA, (k) Noise-free block.

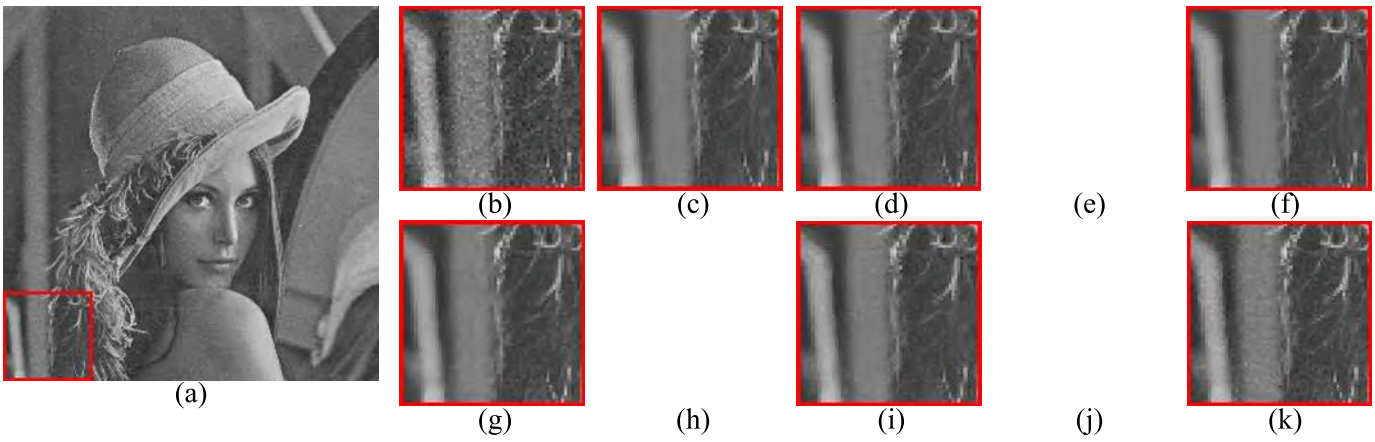

Fig. 13. Performance comparison on the blue channel of Lena image with image details in the zoomed areas (red boxes): (a) The blue channel, (b) Noisy block ($\alpha = 400$), (c) BM3D, (d) BM3DSAPCA, (e) NCSR, (f) WNNM, (g) DnCNN-S, (h) SGHP, (i) AC-PT, (j) ACVA, (k) Noise-free block.

As for the visual texture-preserving performance, ACVA also outperforms the state-of-the-art denoising algorithms. Figs. 12-13 compare the bottom-left corner of the denoising results of image Baboon and Lena. From the zoom-in area, the proposed method outperforms other methods in restoring the special textures of the fur (in Fig. 12) and doorframe (in Fig. 13). In addition, as shown in [46], EFBMD is also inferior to ACVA in preserving the fur texture at the bottom-left corner of image Baboon.

2) Denoising on Real RAW Images: The RAW image of size 3744×5616 is captured by a Canon EOS 5D Mark II. We cut down a 402×402 square from the raw image for denoising tests. The noise parameters (α and b) in Poisson-Gaussian noise model are estimated by the method in [26]. We assume

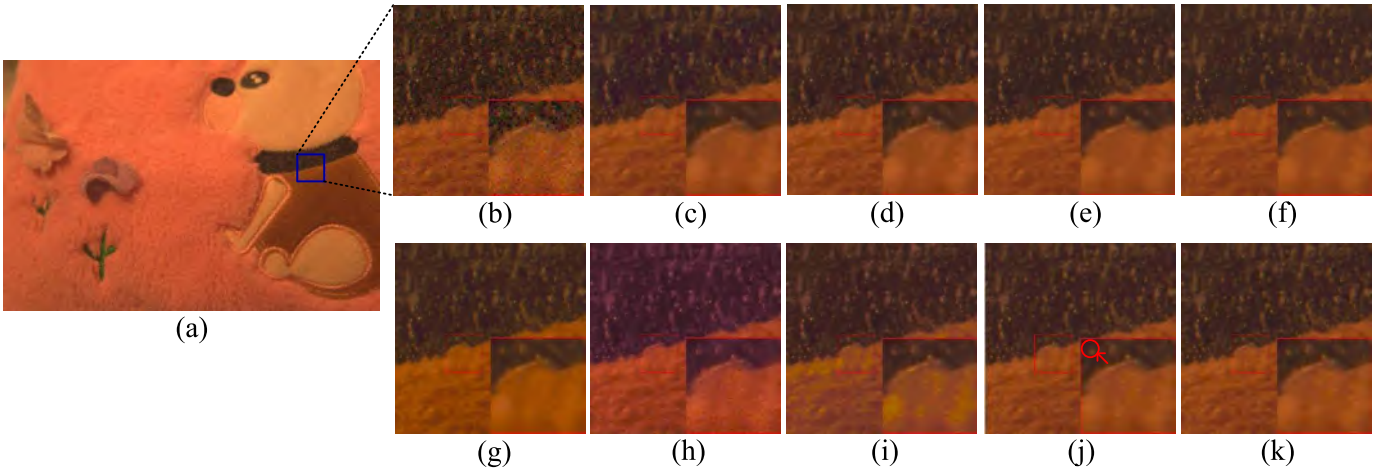

Fig. 14. Denoising the real camera raw image with image details in the zoomed areas (red boxes): (a) Noisy image, (b) Small sample cut down from the blue square, (c) BM3D, (d) BM3DSAPCA, (e) NCSR, (f) WNNM, (g) SLRD, (h) DnCNN-S, (i) SGHP, (j) AC-PT, (k) ACVA.

the noise level is invariant across the whole image. To avoid over-estimate of noise level, we select the top-left 200×200 flat area, estimate its R, G1, G2, B subimage separately, and adopt the minimum estimates of α and b, respectively. After applying the GAT on the RAW image based on the estimated parameters, we denoise the real camera raw image using the considered algorithms directly. To visualize the denoised image, we adopt the method in [47] to transform the results into RGB images.

Fig. 14 shows that ACVA protects zoom-in details (such as singular points and textures) best compared with other algorithms. Specifically, we can also find that there is a noisy black dot mistakenly preserved by AC-PT. And serious color distortion can be observed in the results by SGHP and DnCNN-S, while BM3D, BM3DSAPCA, NCSR, SLRD, and WNNM just blur the isolated white points and brown texture. The serious color distortion by DnCNN-S implies that this state-of-the-art deep learning based denoising algorithm distorts heavily the special textures resulted from the CFA, and how to control this kind of distortion remains an unsolved problem.

VII. Conclusions

In this paper, we have proposed a texture-preserving nonlocal denoising algorithm ACVA. In ACVA, an adaptive clustering method is designed to adaptively and robustly cluster similar patches. A state-of-the-art PCA-based denoising filter is proposed in a transform-domain texture variation adaptive filtering approach to perform a texture-preserving denoising of each cluster. The denoising performance of ACVA is further improved via a sliding window and aggregation approach. When compared with the existing PG techniques (especially the adaptive clustering method in AC-PT), the proposed adaptive clustering method achieves more robust performance at the high noise level. Meanwhile, the proposed DF shows superior denoising performance to other PCA (or SVD) based DFs.

ACVA achieves satisfactory texture-preserving Gaussian denoising performance both quantitatively and visually. Especially on images with irregular textures, ACVA can outperform all the other denoising algorithms tested here in terms of PSNR, SSIM and FSIM results. The noise removal results for camera raw images containing special textures of CFA further verify ACVA's excellent texture-preserving Poisson-Gaussian denoising performance for real application, while the deep learning based denoising algorithm DnCNN works [43] poorly on the real images with CFA patterns that have irregular or stochastic textures. The future work will explore potential benefits of ACVA for improving the overall performance in processing low SNR and low contrast images with irregular textures, such as OCT vessel images [23], low-dose X-ray vessel images [48]–[50] and fluorescence microscopy images [51], [52].

Acknowledgment

The authors would like to thank all the cited authors for providing the source codes used in this work, and the reviewers for their valuable comments on the manuscript.

References

[1] M. Haidekker "Texture Analysis," in *Advanced Biomedical Image Analysis*. Hoboken, NJ, USA: Wiley, 2011, pp. 236–275.
[2] I. Zachevsky and Y. Y. J. Zeevi, "Statistics of natural stochastic textures and their application in image denoising," *IEEE Trans. Image Process.*, vol. 25, no. 5, pp. 2130–2145, May 2016.
[3] A. A. Efros and T. K. Leung, "Texture synthesis by non-parametric sampling," in *Proc. IEEE Int. Conf. Comput. Vis.*, vol. 2, Sep. 1999, pp. 1033–1038.
[4] T. Brox, O. Kleinschmidt, and D. Cremers, "Efficient nonlocal means for denoising of textural patterns," *IEEE Trans. Image Process.*, vol. 17, no. 7, pp. 1083–1092, Jul. 2008.
[5] X. Kang, X. Xiang, S. Li, and J. A. Benediktsson, "PCA-based edge-preserving features for hyperspectral image classification," *IEEE Trans. Geosci. Remote Sens.*, vol. 55, no. 12, pp. 7140–7151, Dec. 2017.
[6] W. Zhao, Y. Lv, Q. Liu, and B. Qin, "Detail-preserving image denoising via adaptive clustering and progressive PCA thresholding," *IEEE Access*, vol. 6, no. 1, pp. 6303–6315, 2018.
[7] K. Mei, B. Hu, B. Fei, and B. Qin. (2018). "Phase asymmetry guided adaptive fractional-order total variation and diffusion for feature-preserving ultrasound despeckling." [Online]. Available: https://arxiv.org/abs/1810.12538
[8] V. Katkovnik, A. Foi, K. Egiazarian, and J. Astola, "From local kernel to nonlocal multiple-model image denoising," *Int. J. Comput. Vis.*, vol. 86, no. 1, p. 1, 2010.
[9] S. Gu, Q. Xie, D. Meng, W. Zuo, X. Feng, and L. Zhang, "Weighted nuclear norm minimization and its applications to low level vision," *Int. J. Comput. Vis.*, vol. 121, no. 2, pp. 183–208, Jan. 2017.

[10] M. Nejati, S. Samavi, H. Derksen, and K. Najarian, "Denoising by low-rank and sparse representations," *J. Vis. Commun. Image Represent.*, vol. 36, no. C, pp. 28–39, Apr. 2016.

[11] K. Dabov, A. Foi, V. Katkovnik, and K. Egiazarian, "Image denoising by sparse 3-D transform-domain collaborative filtering," *IEEE Trans. Image Process.*, vol. 16, no. 8, pp. 2080–2095, Aug. 2007.

[12] L. Zhang, W. Dong, D. Zhang, and G. Shi, "Two-stage image denoising by principal component analysis with local pixel grouping," *Pattern Recognit.*, vol. 43, no. 4, pp. 1531–1549, 2010.

[13] P. Chatterjee and P. Milanfar, "Patch-based near-optimal image denoising," *IEEE Trans. Image Process.*, vol. 21, no. 4, pp. 1635–1649, Apr. 2012.

[14] P. Chatterjee and P. Milanfar, "Clustering-based denoising with locally learned dictionaries," *IEEE Trans. Image Process.*, vol. 18, no. 7, pp. 1438–1451, Jul. 2009.

[15] W. Zuo, L. Zhang, C. Song, D. Zhang, and H. Gao, "Gradient histogram estimation and preservation for texture enhanced image denoising," *IEEE Trans. Image Process.*, vol. 23, no. 6, pp. 2459–2472, Jun. 2014.

[16] Q. Guo, C. Zhang, Y. Zhang, and H. Liu, "An efficient SVD-based method for image denoising," *IEEE Trans. Circuits Syst. Video Technol.*, vol. 26, no. 5, pp. 868–880, May 2016.

[17] S. G. Chang, B. Yu, and M. Vetterli, "Adaptive wavelet thresholding for image denoising and compression," *IEEE Trans. Image Process.*, vol. 9, no. 9, pp. 1532–1546, Sep. 2000.

[18] A. Pizurica and W. Philips, "Estimating the probability of the presence of a signal of interest in multiresolution single- and multiband image denoising," *IEEE Trans. Image Process.*, vol. 15, no. 3, pp. 654–665, Mar. 2006.

[19] F. Luisier, T. Blu, and M. Unser, "A new SURE approach to image denoising: Interscale orthonormal wavelet thresholding," *IEEE Trans. Image Process.*, vol. 16, no. 3, pp. 593–606, Mar. 2007.

[20] A. Foi, V. Katkovnik, and K. Egiazarian, "Pointwise shape-adaptive DCT for high-quality denoising and deblocking of grayscale and color images," *IEEE Trans. Image Process.*, vol. 16, no. 5, pp. 1395–1411, May 2007.

[21] J. Mairal, F. Bach, J. Ponce, G. Sapiro, and A. Zisserman, "Non-local sparse models for image restoration," in *Proc. IEEE Int. Conf. Comput. Vis.*, Sep./Oct. 2010, pp. 2272–2279.

[22] L. Xu, J. Li, Y. Shu, and J. Peng, "SAR image denoising via clustering-based principal component analysis," *IEEE Trans. Geosci. Remote Sens.*, vol. 52, no. 11, pp. 6858–6869, Nov. 2014.

[23] Z. Chen, Y. Mo, P. Ouyang, H. Shen, D. Li, and R. Zhao, "Retinal vessel optical coherence tomography images for anemia screening," *Med. Biol. Eng. Comput.*, vol. 57, no. 4, pp. 953–966, 2018.

[24] J. Chen, J. Benesty, Y. Huang, and S. Doclo, "New insights into the noise reduction Wiener filter," *IEEE Trans. Audio, Speech, Lang. Process.*, vol. 14, no. 4, pp. 1218–1234, Jul. 2006.

[25] V. Katkovnik, "A new method for varying adaptive bandwidth selection," *IEEE Trans. Signal Process.*, vol. 47, no. 9, pp. 2567–2571, Sep. 1999.

[26] A. Foi, M. Trimeche, V. Katkovnik, and K. Egiazarian, "Practical Poissonian-Gaussian noise modeling and fitting for single-image raw-data," *IEEE Trans. Image Process.*, vol. 17, no. 10, pp. 1737–1754, Oct. 2008.

[27] M. Makitalo and A. Foi, "Optimal inversion of the generalized Anscombe transformation for Poisson-Gaussian noise," *IEEE Trans. Image Process.*, vol. 22, no. 1, pp. 91–103, Jan. 2013.

[28] M. Khalilian, F. Z. Boroujeni, N. Mustapha, and M. N. Sulaiman, "K-means divide and conquer clustering," in *Proc. Int. Conf. Comput. Autom. Eng.*, 2009, pp. 306–309.

[29] G. Ahirwar, "A novel K means clustering algorithm for large datasets based on divide and conquer technique," *Pradnyesh J. Bhisikar/Int. J. Comput. Sci. Inf. Technol.*, vol. 5, no. 1, pp. 301–305, 2014.

[30] I. M. Johnstone, "On the distribution of the largest eigenvalue in principal components analysis," *Ann. Statist.*, vol. 29, no. 2, pp. 295–327, 2001.

[31] J. Bigot, C. Deledalle, and D. Féral, "Generalized SURE for optimal shrinkage of singular values in low-rank matrix denoising," *J. Mach. Learn. Res.*, vol. 18, no. 1, pp. 4991–5040, 2016.

[32] H. Liu, P. Sun, Q. Du, Z. Wu, and Z. Wei, "Hyperspectral image restoration based on low-rank recovery with a local neighborhood weighted spectral–spatial total variation model," *IEEE Trans. Geosci. Remote Sens.*, vol. 57, no. 3, pp. 1409–1422, Mar. 2018.

[33] F. Zhu *et al.*, "Reducing Poisson noise and baseline drift in X-ray spectral images with bootstrap Poisson regression and robust nonparametric regression," *Phys. Med. Biol.*, vol. 58, no. 6, p. 1739, 2013.

[34] M. Köhler, A. Schindler, and S. Sperlich, "A review and comparison of bandwidth selection methods for kernel regression," *Int. Stat. Rev.*, vol. 82, no. 2, pp. 243–274, 2014.

[35] B. Qin, Z. Shen, Z. Fu, Z. Zhou, Y. Lv, and J. Bao, "Joint-saliency structure adaptive kernel regression with adaptive-scale kernels for deformable registration of challenging images," *IEEE Access*, vol. 6, no. 1, pp. 330–343, 2018.

[36] B. Qin, Z. Shen, Z. Zhou, J. Zhou, and Y. Lv, "Structure matching driven by joint-saliency-structure adaptive kernel regression," *Appl. Soft Comput.*, vol. 46, pp. 851–867, Sep. 2016.

[37] A. Olmos and F. A. A. Kingdom, "A biologically inspired algorithm for the recovery of shading and reflectance images," *Perception*, vol. 33, no. 12, pp. 1463–1473, 2004.

[38] A. G. Weber. *The USC-SIPI Image Database*. Accessed: Aug. 10, 2017. [Online]. Available: http://sipi.usc.edu/services/database/Database.html

[39] Q. Huynh-Thu and M. Ghanbari, "Scope of validity of PSNR in image/video quality assessment," *Electron. Lett.*, vol. 44, no. 13, pp. 800–801, Jun. 2008.

[40] Z. Wang, A. C. Bovik, H. R. Sheikh, and E. P. Simoncelli, "Image quality assessment: From error visibility to structural similarity," *IEEE Trans. Image Process.*, vol. 13, no. 4, pp. 600–612, Apr. 2004.

[41] L. Zhang, L. Zhang, X. Mou, and D. Zhang, "FSIM: A feature similarity index for image quality assessment," *IEEE Trans. Image Process.*, vol. 20, no. 8, pp. 2378–2386, Aug. 2011.

[42] W. Dong, L. Zhang, G. Shi, and X. Li, "Nonlocally centralized sparse representation for image restoration," *IEEE Trans. Image Process.*, vol. 22, no. 4, pp. 1620–1630, Apr. 2013.

[43] K. Zhang, W. Zuo, Y. Chen, D. Meng, and L. Zhang, "Beyond a Gaussian denoiser: Residual learning of deep CNN for image denoising," *IEEE Trans. Image Process.*, vol. 26, no. 7, pp. 3142–3155, Jul. 2017.

[44] M. Gavish and D. L. Donoho, "The optimal hard threshold for singular values is $4/\sqrt{3}$," *IEEE Trans. Inf. Theory*, vol. 60, no. 8, pp. 5040–5053, Jun. 2014.

[45] M. Gavish and D. L. Donoho, "Optimal shrinkage of singular values," *IEEE Trans. Inf. Theory*, vol. 63, no. 4, pp. 2137–2152, Apr. 2014.

[46] C.-C. Yang, S.-M. Guo, and J. S.-H. Tsai, "Evolutionary fuzzy block-matching-based camera raw image denoising," *IEEE Trans. Cybern.*, vol. 47, no. 9, pp. 2862–2871, Sep. 2017.

[47] D. Khashabi, S. Nowozin, J. Jancsary, and A. W. Fitzgibbon, "Joint demosaicing and denoising via learned nonparametric random fields," *IEEE Trans. Image Process.*, vol. 23, no. 12, pp. 4968–4981, Dec. 2014.

[48] M. Jin, R. Li, J. Jiang, and B. Qin, "Extracting contrast-filled vessels in X-ray angiography by graduated RPCA with motion coherency constraint," *Pattern Recognit.*, vol. 63, pp. 653–666, Mar. 2017.

[49] M. Jin, D. Hao, S. Ding, and B. Qin, "Low-rank and sparse decomposition with spatially adaptive filtering for sequential segmentation of 2D+t vessels," *Phys. Med. Biol.*, vol. 63, no. 17, 2018, Art. no. 17LT01.

[50] B. Qin *et al.*, "Accurate vessel extraction via tensor completion of background layer in X-ray coronary angiograms," *Pattern Recognit.*, vol. 87, pp. 38–54, Mar. 2019.

[51] M. Weigert *et al.*, "Content-aware image restoration: Pushing the limits of fluorescence microscopy," *Nature Methods*, vol. 15, no. 12, p. 1090, 2018.

[52] R. Li, Y. Wang, H. Xu, B. Fei, and B. Qin, "Micro-droplet detection method for measuring the concentration of alkaline phosphatase-labeled nanoparticles in fluorescence microscopy," *Sensors*, vol. 17, no. 11, p. 2685, 2017.

Wenzhao Zhao received the B.Sc. degree in bioengineering from Yangzhou University, Yangzhou, in 2013, and the M.Sc. degree in biomedical engineering from Shanghai Jiao Tong University, Shanghai, China, in 2018. His current research interests include image processing and computer vision.

Qiegen Liu (M'16) received the B.S. degree in applied mathematics from Gannan Normal University, and the M.Sc. degree in computation mathematics and the Ph.D. degree in biomedical engineering from Shanghai Jiao Tong University (SJTU). From 2015 to 2017, he held a post-doctoral position with UIUC and the University of Calgary. Since 2012, he has been with School of Information Engineering, Nanchang University, Nanchang, China, where he is currently an Associate Professor. His current research interest is sparse representations, deep learning and their applications in image processing, computer vision, and MRI reconstruction.

Yisong Lv received the M.Sc. degree in automatic instruments from the Kunming University of Science and Technology, Kunming, in 1999, and the Ph.D. degree in biomedical engineering from Shanghai Jiao Tong University, Shanghai, China, in 2003. His current research interests include image analysis, machine learning, and computer vision.

Binjie Qin (M'07) received the M.Sc. degree in measuring and testing technologies and instruments from the Nanjing University of Science and Technology, Nanjing, and the Ph.D. degree in biomedical engineering from Shanghai Jiao Tong University, Shanghai, China, in 1999 and 2002, respectively. He was a Lecturer and an Associate Professor with the Department of Biomedical Engineering, School of Life Sciences and Biotechnology, Shanghai Jiao Tong University, Shanghai, China. From 2012 to 2013, he was a Visiting Professor with the Department of Computer Science, University College London, U.K. He is currently an Associate Professor with the School of Biomedical Engineering, Shanghai Jiao Tong University, Shanghai, China. His current research interests include biomedical imaging, image processing, machine learning, computer vision, and biomedical instrumentation.